Correspondence to:

Y. Yang,
yyang2@xmu.edu.cn

Characteristics and Dynamics of the Interannual Eddy Kinetic Energy Variation in the Central Pacific Sector of the Southern Ocean

Guanqi Fu[1,2] , Yang Yang[1] , X. San Liang[3,4] , and Yuhui Zhao[2,3]

[1]State Key Laboratory of Marine Environmental Science, College of Ocean and Earth Sciences, Xiamen University, Xiamen, China, [2]School of Marine Sciences, Nanjing University of Information Science and Technology, Nanjing, China, [3]The Artificial Intelligence Group, Division of Frontier Research, Southern Marine Laboratory, Zhuhai, China, [4]Department of Atmospheric and Oceanic Sciences, and Institute of Atmospheric Sciences, Fudan University, Shanghai, China

Abstract Mesoscale eddies play a crucial role in the dynamical balance of the Southern Ocean (SO) circulation. Yet, it remains unclear why the SO transient eddy activity has significant variations on interannual time scales, and to what extent these low-frequency variations are attributed to wind forcing changes. Here we use a functional analysis tool, namely, the multiscale window transform (MWT), the MWT-based theory of canonical transfer and a time-dependent energetics framework to investigate these issues. Our focus is on the central Pacific sector of the SO in which there is a significant time-mean and interannual variability of the eddy kinetic energy (EKE). It is found that wind stress does not directly contribute to the interannual EKE variability through wind power injection to the eddies; instead, the influence is fulfilled indirectly through two internal pathways. First, the baroclinic pathway in which the wind-generated mean kinetic energy (MKE) is converted to the mean available potential energy (APE), and is further released to eddy APE and finally to EKE through baroclinic instability, is the dominant one. Second, the barotropic pathway, in which MKE directly fuels EKE through barotropic instability, is faster but secondary, and its influence is only concentrated along the axis of the Antarctic Circumpolar Current. Our results highlight the dynamical connections between the internal and external processes in the SO energy system, and provide insights into the predictability of the SO eddies on interannual time scales.

Plain Language Summary The strength of the transient eddy activity in the Southern Ocean (SO) exhibits considerable variability on interannual time scales. Although the SO eddies respond to wind forcing, it remains unclear how the wind stress modulates the internal oceanic processes, for example, instabilities, and how it determines the low-frequency variability of the eddy activity. Using a novel time-dependent energetics framework, we find that wind stress does not directly control the interannual eddy kinetic energy (EKE) variability by wind power injection to the eddies; instead, we identify two possible internal energy pathways in the central Pacific sector of the SO. First, the baroclinic pathway is the dominant, in which the wind-generated mean kinetic energy (MKE) is converted to the available potential energy, and finally released to EKE through baroclinic instability. Second, the barotropic pathway, in which the MKE directly fuels EKE through barotropic instability, is much faster but secondary. This study provides insights into understanding the energy pathways by connecting the external forcing and internal processes that together determine the low-frequency variation of the eddy activity in the SO.

1. Introduction

The Southern Ocean (SO) is one of the most eddy-rich regions of the world's ocean (Frenger et al., 2015; Fu et al., 2010). It has been well recognized that mesoscale eddies play a fundamental role in the dynamical balance of the SO circulation. They greatly modulate the transport and mixing of tracers as well as the redistribution of momentum, heat flux, and energy (Sallée et al., 2008; Tamsitt et al., 2016; Wilson et al., 2015; Xu et al., 2022). In addition, since the SO connects the Indian Ocean, the Pacific Ocean and the Atlantic Ocean, it functions as the main channel for exchanging climate signals among the three ocean basins (Sokolov & Rintoul, 2009).

Influenced by the westerly belt over the SO, the Antarctic Circumpolar Current (ACC) is characterized by a complex jet front structure, providing favorable conditions for eddy generation (Fu et al., 2010; Sokolov & Rintoul, 2009). Since the satellite altimetry era (1993 to present), one of the most conspicuous climate changes
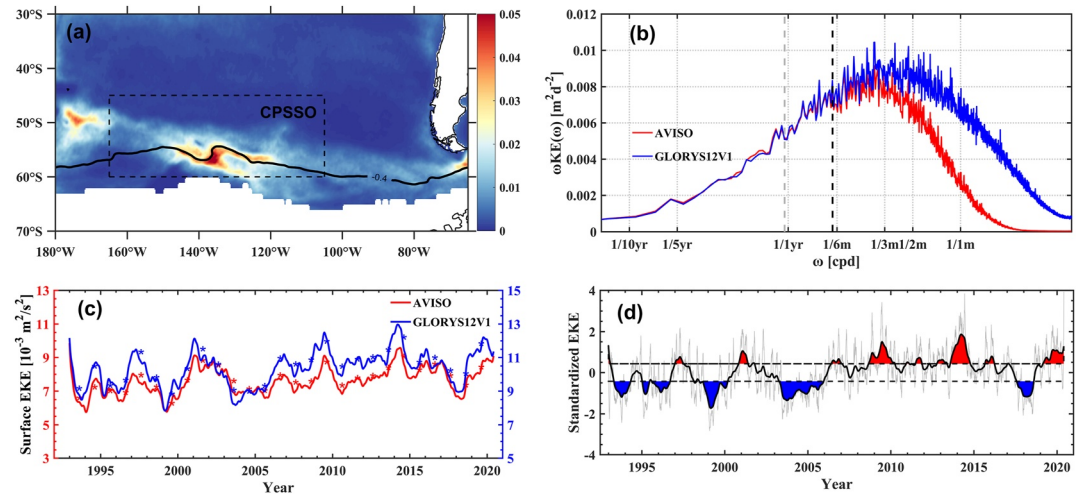
Figure 1. (a) Long-term mean surface geostrophic Eddy kinetic energy (EKE) (b; m²/s²) in the central and east Pacific sector of the Southern Ocean based on the Archiving, Validation, and Interpretation of Satellite Oceanographic (AVISO) data set. The rectangular box enclosed by dashed lines marks the study region. The solid black line in panel (a) shows the jet axis (−0.4-m isobaths of the absolute dynamic topography). (b) Variance-preserving geostrophic KE spectra averaged over the central Pacific sector of the Southern Ocean (CPSSO) based on AVISO (solid red line) and Global Ocean Reanalysis Simulations Data (GLORYS12V1) (solid blue line). The dashed lines denote the period of 192 days (black) and 384 days (gray). (c) Surface geostrophic EKE time series averaged over the CPSSO from AVISO (red) and GLORYS12V1 (blue). Both the time series are 1-year low-pass filtered. The asterisks represent the annual-mean values. (d) Time series of the standardized area-mean EKE vertically integrated from surface to 1,000 m. Solid gray and solid black lines show the raw and 1-year low-pass filtered series respectively. The two dashed lines denote the 0.6 and −0.6 standard deviation of the filtered EKE, respectively. Red (blue) shadings mark the periods for high (low) EKE composites.

in the SO is an apparent increasing trend of the Southern Annular Mode, which is associated with the increase of wind stress speed over the SO (Lin et al., 2018). Interestingly, the Eddy Kinetic Energy (EKE) in the SO has also been found to exhibit significant interannual variability as well as a long-term increasing trend (Hogg et al., 2015). A rich literature addresses the mechanism that controls the low-frequency variation of EKE in the SO. Meredith and Hogg (2006) first reported that wind stress leads the EKE by approximately 1–3 years in the SO. The follow-up studies further found that the time mean transport is insensitive to the increase in wind stress because the transient field readjusts to the wind (Hogg et al., 2015; Marshall et al., 2017; Menna et al., 2020; Meredith & Hogg, 2006). This phenomenon has been known as "eddy saturation" (Straub, 1993). Several studies suggested that the response of the eddy activity to the increasing wind stress over the SO has a stronger finger-print in the Pacific and Indian sectors than in the Atlantic sector (Hogg et al., 2015; Menna et al., 2020; Meredith & Hogg, 2006). Recently, Zhang et al. (2021) revisited this problem using altimetry crossover measurements and reported that no coherent increase of EKE is observed over the entire SO. They stressed that significantly increasing EKE trends are only concentrated in a few regions, especially in the regions south of New Zealand and downstream of the Campbell Plateau (Figure 1a).

Although wind stress has been considered as the major contributor to the low-frequency variation of EKE in the SO (Hogg et al., 2015; Meredith & Hogg, 2006), it has been recently noted by Cai et al. (2022) that the spatial pattern of the EKE change does not necessarily match that of the wind stress. The spatial inhomogeneity of EKE and its associated generation mechanism in the SO have been well studied. Several previous studies suggested that bottom topography plays a key role in generating standing meanders of the ACC, which are associated with localized regions of high EKE (Barthel et al., 2017, 2022; Cai et al., 2022; Thompson & Sallée, 2012). Both baroclinic instability and barotropic instability are found to be responsible for the EKE generation in these highly localized regions (Wilson et al., 2015; Youngs et al., 2017). In addition to instability processes, non-local processes such as spatial advection and pressure work could also significantly influence the EKE variability in a localized ocean sector (Grooms et al., 2013; Huang et al., 2023; Yang et al., 2021). Also, it has been suggested that the direct wind stress work on mesoscale eddies usually functions to damp the eddies and is small in magnitude in the EKE budget of mesoscale eddies (Renault et al., 2017; Xu et al., 2016). These results suggest that the low-frequency EKE variation in the SO may not be directly controlled by the external wind forcing, but may

rather be modulated by oceanic processes such as instability and non-local processes. Note that the external forcing and internal oceanic processes are not mutually exclusive as the wind stress can spin up the mean flow, which becomes unstable and produces EKE (Hogg & Blundell, 2006). Recently, Hogg et al. (2022) investigated the role of the intrinsic (chaotic) and wind-forced processes in determining the EKE in the SO using an ensemble of simulations. They found that the EKE variation in the SO is mostly random, even on the interannual timescale. Up to now, it remains unclear how the EKE in the SO is modulated by the external wind forcing and internal instability processes at the interannual time scale. In this study, we aim to investigate this problem using a novel time-varying multiscale energetics framework. The energetics framework invokes the use of a localized scale-decomposition technique, namely, the multiscale window transform (MWT; Liang & Anderson, 2007), and the MWT-based theory of canonical transfer (Liang, 2016).

The rest of this paper is organized as follows. We describe the data used for this study in Section 2, introduce the method in Section 3, present the major results in Section 4, and, finally, summarize the whole study in Section 5.

2. Data

2.1. Data Description

Satellite altimeter observation has greatly enhanced our knowledge of the SO eddies and their associated EKE. However, it only yields information on the sea surface and hence cannot give information in the vertical water column. In contrast, eddy-resolving model solutions can provide a four-dimensional view of the eddy fields. To this end, we use the 1/12° Global Ocean Reanalysis Simulations Data (GLORYS12V1) distributed by Copernicus Marine and Environment Monitoring Service (CMEMS) as the main data set to study the time-varying energetics in the region of interest. The GLORYS12V1 product has a horizontal resolution of 1/12° and 50 vertical levels, covering the entire altimetry era (1993 onward). Considering that the EKE and its associated energetic processes are mostly confined in the upper 1,000 m (Storch et al., 2012), we only use the upper 36 layers (0–1,062 m) of the model outputs. In our analysis, daily fields including velocity, temperature, salinity and sea surface height (SSH) from January 1993 to May 2020 are used.

To validate the GLORYS12V1 reanalysis output in the study region, the satellite-based merged absolute dynamic topography provided by the Archiving, Validation, and Interpretation of Satellite Oceanographic (AVISO) data is also used (Ducet et al., 2000). In addition, the wind stress data from the European Center for Medium-Range Weather Forecasting interim reanalysis (ERA-Interim, 1993–2018) and the ERA5 (2019–2020) reanalysis, which is also the forcing fields of the GLORYS12V1 simulation, is used to estimate the wind power input into the background flow and the eddies. Both the altimetry and wind stress data have been interpolated onto the same horizontal grid points as the GLORYS12V1 data, and all used data have the same time coverage (i.e., January 1993–May 2020).

Previous observational studies reported that the strongest response of EKE to the wind stress change occurs in the Pacific sector of the SO (Hogg et al., 2015; Menna et al., 2020; Morrow et al., 2010). Figure 1a displays the time-mean surface geostrophic EKE (definition is given in Section 3.1) in the Pacific sector. It can be seen that EKE maximizes in the central Pacific sector of the SO (CPSSO, 165°−105°W, 45°−60°S; the black dotted box in Figure 1a), where the mean ACC takes a large-amplitude meandering path. Considering that the observed EKE in this particular region exhibits a significant interannual component as reported in previous studies (e.g., Zhang et al., 2021), we focus on the mechanism of the interannual eddy energetics in this region.

2.2. Data Validation and Composite Definition

To examine the performance of GLORYS12V1, we compare the surface geostrophic EKE evolutions over the past 27 years obtained from the two data sets. Figure 1c presents the 1-year low-pass filtered time series of EKE averaged over the CPSSO (rectangular box in Figure 1a). It shows that the time series calculated from GLORYS12V1 agrees well with that from AVISO. The correlation coefficient between the two time series reaches 0.85 and 0.88 before and after filtering, respectively. The consistency demonstrates that the GLORYS12V1 data set successfully reproduced the temporal evolution of observed EKE in the CPSSO.

We use the time series of the standardized area-averaged and vertically integrated (0–1,000 m) EKE as the index of the eddy activity in this region (Figure 1d). High (Low) EKE phase is defined when the index is greater (less)

than 0.6 (−0.6) standard deviation. Based on this definition, 970 and 995 snapshots are selected for the high- and low-EKE states, respectively. We choose ±0.6 as the threshold in order to include sufficient sampling years in the composite analysis. Other thresholds, such as ±0.8 and ±1, have also been tried and the results are similar to the ±0.6 case.

3. Methods

3.1. Multiscale Window Transform (MWT) and Multiscale Energy

The time-varying energetics framework employed in this study is based on the multiscale window transform (MWT) developed by Liang and Anderson (2007). The MWT is a functional analysis tool that allows for the partitioning of a function space into mutually orthogonal subspaces (hereafter referred to as scale windows), each with an exclusive range of scales. It is common in literature to use Reynolds decomposition to divide a field into its mean (usually time-mean) and fluctuating components. This approach is not suitable for investigation of highly localized and/or nonstationary processes. To overcome this difficulty, many researchers tried to use filters (e.g., $u(t) = \bar{u}(t) + u'(t)$, where $\bar{u}(t)$ and $u'(t)$ stand for the slowly evolving mean field and faster-evolving eddy field) and then take the square of the filtered component as the energy of that component (e.g., $[\bar{u}(t)]^2$ and $[u'(t)]^2$). Liang (2016) showed that using $[u'(t)]^2$ as the time-varying energy of the eddy field is problematic because $u^2 \neq \bar{u}^2 + u'^2$. That is to say, the above decomposition fails to guarantee the conservation of the total energy. In fact, multiscale energy is a concept in phase space (think about the Fourier power spectrum). So it is actually not a trivial problem to obtain a physically consistent presentation of the time-dependent multiscale energy. In fact, it is a rather difficult problem until the filter bank and the wavelet are connected (Strang & Nguyen, 1996). Liang and Anderson (2007) developed the MWT for this very purpose.

Different from traditional filters, MWT not only outputs reconstructions (filtered fields), it also yields transform coefficients which are essential to represent the local energy of the filtered fields. For example, in this study, we need two scale windows, namely, the background flow window and the eddy window (the definition of each window is given below). A state variable, say, $u(t)$, then can be decomposed as

$$u(t) = u^{\sim 0}(t) + u^{\sim 1}(t),\tag{1}$$

where $u^{\sim 0}$ and $u^{\sim 1}$ stand for reconstructions on the background flow window and the eddy window, respectively. In the MWT framework, for each reconstruction $u^{\sim \varpi}(t)$ ($\varpi = 0, 1$), there exists a corresponding transform coefficient, $\hat{u}_n^{\sim \varpi}$ (n denotes the discrete time step and the hat is the transform operator). The very transform coefficient, which is defined in the phase space and is not yielded by general filters, allows for a faithful representation of energy on window ϖ. Liang and Anderson (2007) proved that the energy of u on scale window ϖ at time step n is $(\hat{u}_n^{\sim \varpi})^2$ (up to some constant). Note that $(\hat{u}_n^{\sim \varpi})^2$ is by no means equal to $[u^{\sim \varpi}(t)]^2$. It's worth mentioning that orthogonality is essential in defining the multiscale energy (Liang & Anderson, 2007). Nonorthogonal decompositions are found to introduce spurious temporal variations of the eddy energy (Kang & Curchitser, 2017).

To determine the cutoff frequency that divides the two scale windows, we plot in Figure 1b the surface geostrophic kinetic energy (KE) power spectra averaged over the CPSSO. It can be seen that there are significant multi-time-scale signals in this region. The mesoscale signals are mainly concentrated in the window between 60 and 180 days (Figure 1b). Frenger et al. (2015) analyzed the statistical features of the mesoscale eddies in the SO. They found that the life span of mesoscale eddies in this region is generally shorter than 25 weeks. Long-live eddies with a life span over 1 year in the whole SO is less than 1%. Based on the eddy statistics and what we have learned from the KE spectrum, we choose a cutoff period of 192 days to separate the original field into a slowly varying background flow (with a period longer than 192 days, including the time mean field) and a high-frequency eddy field (with period shorter than 192 days). Notice that the MWT requires the cutoff period to be a power of 2 (Liang & Anderson, 2007). Figure 2 displays the instantaneous maps of the original SSH and its reconstructions on two typical days from the simulation. It can be seen that the reconstructed background flow captures the frontal structures of the ACC. More importantly, it is nonstationary. A simple Reynolds time-mean-eddy decomposition does not yield a time-dependence background flow and therefore is not suitable for investigating the interannual variation of EKE. The mesoscale eddies are well separated from the background flow and are mainly concentrated along the jet front. The above results confirm that the cutoff period of 192 days is reasonable. We have also tested 384 and 96 days as the cutoff period and found that the results are similar to the 192-day case.
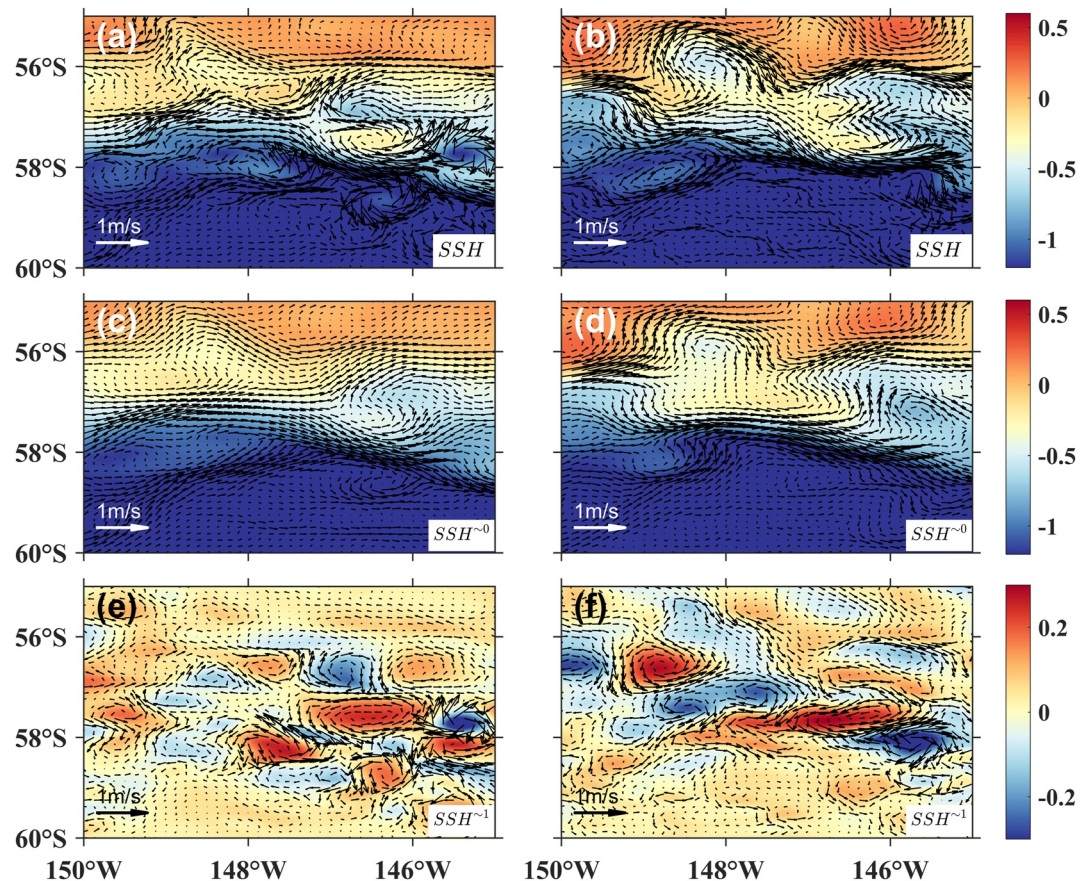
Figure 2. Snapshots of sea surface height (SSH) (m) on 14 January 1996 (the left column) and 15 January 2014 (the right column). The first row (a and b) represents the original SSH field simulated by GLORYS12V1; the second row (c and d) and the third row (e and f) represent the SSH fields reconstructed by multiscale window transform on the background flow window ($SSH^{\sim 0}$) and the eddy window ($SSH^{\sim 1}$), respectively.

It should be noted that in this study we focus on the interannual variations of KE associated with transient eddies (i.e., perturbations with periods shorter than 192 days). The standing meander, another important feature in the AAC system, is mostly included in the background flow field because they have much longer temporal scale. It's important to realize that the standing meanders and transient eddies are two distinct dynamical components of the ACC system. Besides their different temporal variability (slow vs. fast), previous studies have shown that the two also have a clear scale separation regarding their length scale (Held, 1983). The standing meander has a wavelength of approximately 500 km, whereas the transient mesoscale eddies generally have length scales of ~50–200 km in the SO (Chapman et al., 2015; Held, 1983; Williams et al., 2007). Dynamically, the standing meanders are generated by the interaction of the ACC jets with large-scale topography (Hughes, 2005), whereas the transient eddies, collocated with the meander region (i.e., the so-called storm track in the ocean), are generated due to baroclinic and barotropic instabilities of the meandering jet (Abernathey & Cessi, 2014; Bischoff & Thompson, 2014; Chapman et al., 2015). In other words, the standing meanders of the ACC provide favorable background environment for the formation of transient eddies. Therefore, we treat the standing meanders, which are larger in length scale and lower in frequency, as the background flow in this study, consistent with the above-cited works.

Also note that in this study we choose to separate these two dynamical processes in temporal scale rather than in spatial scale because the former is more convenient and it works fine in our case, as was done in several studies in this field (e.g., Chapman et al., 2015; Williams et al., 2007). The so-obtained mesoscale window inevitably include signals with large spatial-scale (order of 1,000 km) but short time-sale (<2 weeks), due to forcing by transient storms. Future studies are needed to consider these processes separately using scale decomposition technique both in the temporal and spatial domain.

With MWT, the KE and available potential energy (APE) on window ϖ ($\varpi = 0, 1$) are

$$K^{\varpi} = \frac{1}{2}\left(\hat{\boldsymbol{v}}_h^{\sim\varpi} \cdot \hat{\boldsymbol{v}}_h^{\sim\varpi}\right) \tag{2}$$

and

$$A^{\varpi} = \frac{g^2}{2\rho_0^2 N^2}(\hat{\rho}^{\sim\varpi})^2, \tag{3}$$

where $\rho_0 = 1025$ kg/m^3 is the constant reference density, $\boldsymbol{v}_h$ the horizontal velocity, N the buoyancy frequency, g the gravitation acceleration, and ρ the density anomaly from a reference state $\rho_r(z)$ which is defined as the time- and area-mean density at each depth. For easy reference, K^0 and K^1, that is, KE on background flow and eddy window, are denoted as mean kinetic energy (MKE) and EKE, respectively. Readers should be aware that the time-dependent MKE and EKE defined in this study are different from the conventional ones (such as those defined by the Reynolds decomposition) appearing in literature. Similarly, A^0 and A^1, that is, APE on the background flow and eddy window, are denoted as MAPE and EAPE, respectively.

3.2. Canonical Transfer and Time-Dependent Multiscale Energetics Analysis

Energy transfer between different scale windows is fundamental in a multiscale ocean current system. A faithful representation of this process is thus of key importance. The canonical transfer was first introduced within the framework of the MWT by Liang and Robinson (2005) (called "perfect transfer" then), and was later rigorously derived in Liang (2016). Consider a scalar field T in an incompressible flow $\boldsymbol{v}$, the canonical transfer is proved to be

$$\Gamma_n^{\varpi} = \frac{1}{2}\left[\widehat{(\boldsymbol{v}T)}_n^{\sim\varpi} \cdot \nabla\hat{T}_n^{\sim\varpi} - \hat{T}_n^{\sim\varpi}\nabla \cdot \widehat{(\boldsymbol{v}T)}_n^{\sim\varpi}\right]. \tag{4}$$

Liang (2016) realized that Equation 4 bears a Lie bracket form and satisfies the Jacobian identity, reminiscent of the Poisson bracket in Hamiltonian mechanics. Most importantly, Equation 5 satisfies the following conservation property:

$$\sum_{\varpi}\sum_n \Gamma_n^{\varpi} = 0, \tag{5}$$

which means that the canonical transfer merely redistributes energy among scale windows. However, the property does not hold in traditional formalisms (see Liang (2016) for details).

Based on the MWT and the canonical transfer theory, Liang (2016) derived the multiscale KE and APE budget equations from the primitive equations:

$$\frac{\partial K^{\varpi}}{\partial t} = -\nabla \cdot Q_K^{\varpi} - \nabla \cdot Q_P^{\varpi} - b^{\varpi} + \Gamma_K^{\varpi} + F_K^{\varpi}, \tag{6}$$

$$\frac{\partial A^{\varpi}}{\partial t} = -\nabla \cdot Q_A^{\varpi} + b^{\varpi} + \Gamma_A^{\varpi} + F_A^{\varpi}. \tag{7}$$

The definition and physical meaning of each term are referred to Table 1. Notice that all terms in Equations 6 and 7 are four-dimensional field variables and hence allow us to examine the spatio-temporal variations of the energetic processes. Γ_K^{ϖ} and Γ_A^{ϖ} represent the canonical transfer of KE and APE, respectively. For convenience, we will use $\Gamma_K^{0\rightarrow1}$ ($\Gamma_A^{0\rightarrow1}$) to denote the canonical KE (APE) transfer from the background flow window to the eddy window. As established in Liang and Robinson (2005), positive $\Gamma_K^{0\rightarrow1}$ ($\Gamma_A^{0\rightarrow1}$) means transfer of KE (APE) from the background flow to the eddies, indicative of the occurrence of barotropic (baroclinic) instability.

The external wind forcing is examined by the energy exchange between the wind stress and the surface current. Using MWT, the rate of wind work on window ϖ is:

$$WW^{\varpi} = \frac{1}{\rho_0}\hat{\boldsymbol{v}}_0^{\sim\varpi} \cdot \hat{\boldsymbol{\tau}}^{\sim\varpi}, \tag{8}$$

Table 1
Expressions of Terms in Equations 6 and 7 on Window ϖ

Term	Mathematical expression	Physical interpretation
$\partial K^{\varpi}/\partial t$	$\frac{\partial}{\partial t}\left(\frac{1}{2}\hat{\boldsymbol{v}}_h^{\sim\varpi}\cdot\hat{\boldsymbol{v}}_h^{\sim\varpi}\right)$	Tendency of KE on scale window ϖ
$\partial A^{\varpi}/\partial t$	$\frac{\partial}{\partial t}\left[\frac{g^2}{2\rho_0^2 N^2}(\hat{\rho}^{\sim\varpi})^2\right]$	Tendency of APE on scale window ϖ
Q_K^{ϖ}	$\left[\widehat{(\boldsymbol{vv}_h)}^{\sim\varpi}\cdot\hat{\boldsymbol{v}}_h^{\sim\varpi}\right]/2$	KE flux on scale window ϖ
Q_P^{ϖ}	$\frac{1}{\rho_0}\hat{\boldsymbol{v}}^{\sim\varpi}\hat{p}^{\sim\varpi}$	Pressure flux on scale window ϖ
Q_A^{ϖ}	$\left[\frac{g^2}{\rho_0^2 N^2}\hat{\rho}^{\sim\varpi}\widehat{(\boldsymbol{v}\rho)}^{\sim\varpi}\right]/2$	APE flux on scale window ϖ
b^{ϖ}	$g\hat{\rho}^{\sim\varpi}\hat{w}^{\sim\varpi}/\rho_0$	Buoyancy (APE-to-KE) conversion on scale window ϖ
Γ_K^{ϖ}	$\left[\widehat{(\boldsymbol{vv}_h)}^{\sim\varpi}:\nabla\hat{\boldsymbol{v}}_h^{\sim\varpi}-\nabla\cdot\widehat{(\boldsymbol{vv}_h)}^{\sim\varpi}\cdot\hat{\boldsymbol{v}}_h^{\sim\varpi}\right]/2$	Canonical transfer of KE to scale window ϖ
Γ_A^{ϖ}	$\frac{g^2}{\rho_0^2 N^2}\left[\widehat{(\boldsymbol{v}\rho)}^{\sim\varpi}\cdot\nabla\hat{\rho}^{\sim\varpi}-\hat{\rho}^{\sim\varpi}\nabla\cdot\widehat{(\boldsymbol{v}\rho)}^{\sim\varpi}\right]/2$	Canonical transfer of APE to scale window ϖ
$F_K^{\varpi},F_A^{\varpi}$	-	Residues

Note. The derivation of the equations and meaning of each mathematical symbol are referred to Liang (2016).

where $\boldsymbol{v}_0$ is the surface horizontal velocity, and $\boldsymbol{\tau}$ the surface wind stress. The wind stress is computed using the bulk formulae by considering the relative motion between the surface wind and the ocean surface current (e.g., Renault et al., 2017). When calculating the wind work on the eddy window (WW[1]), we use the geostrophic velocity instead of the full velocity because the wind work on the ageostrophic motions is much larger in magnitude than that on the geostrophic currents (e.g., mesoscale eddies). This dominant ageostrophic part of wind power input has long been recognized to be mostly dissipated in the Ekman layer with negligible contributions to the mesoscale eddies (Renault et al., 2017; Wunsch, 1998).

4. Results

4.1. Spatiotemporal Characteristics of EKE

Figure 3 displays the long-term mean surface KE on the background-flow window and the eddy window, calculated using both AVISO and GLORYS12V1 data sets. Before examining the EKE distributions, it is necessary to look at the background flows. According to the satellite observation (Figure 3a), the ACC in the CPSSO holds
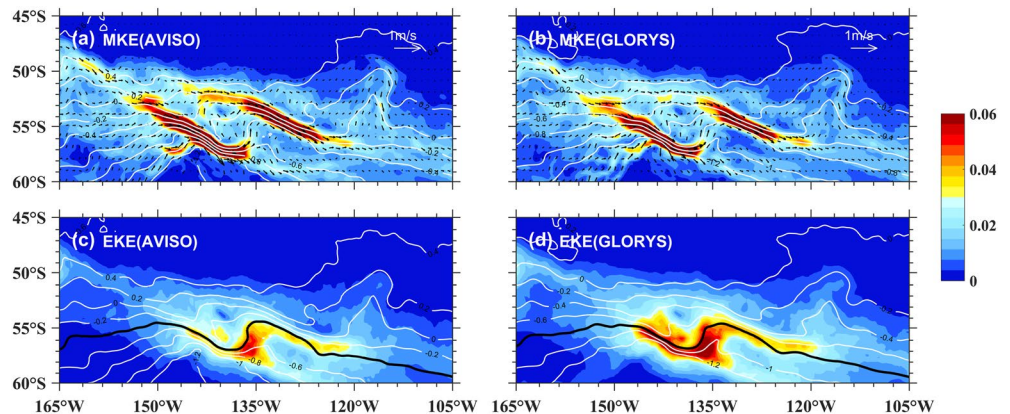

Figure 3. Long-term mean maps of the surface mean kinetic energy (MKE) (colored shading; m^2/s^2), surface horizontal geostrophic velocity (vectors; m/s) and absolute dynamic topography (contours; m) based on panel (a) Archiving, Validation, and Interpretation of Satellite Oceanographic and panel (b) Global Ocean Reanalysis Simulations Data data sets. Panels (c), (d) as in panels (a), (b), but for the surface Eddy kinetic energy (EKE) (m^2/s^2). The black lines in panels (c) and (d) show the jet axis. Note that both the MKE and EKE in this figure are calculated by the geostrophic flow for the convenience of comparison between the two data sets.
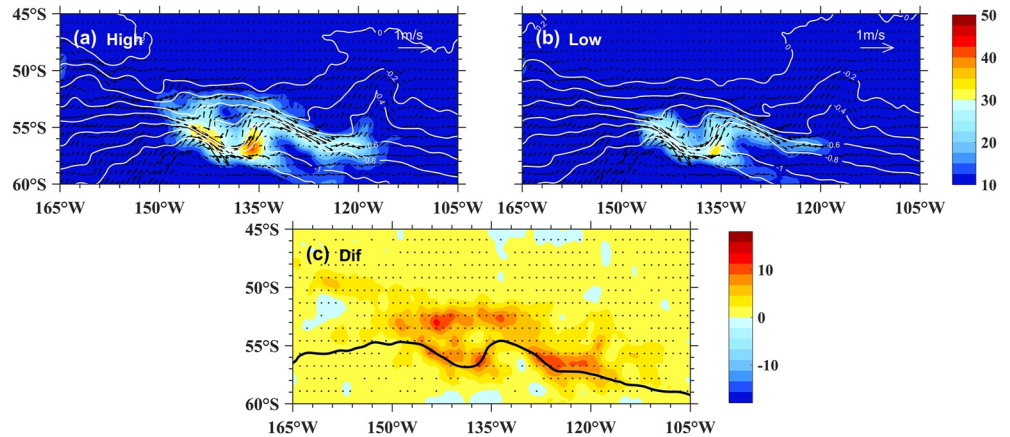
Figure 4. Composite maps of the depth-integrated (0–1,000 m) Eddy kinetic energy (colored shading; m^3/s^2) along with sea surface height (contours; m) and surface circulation (vectors; m/s) for (a) the high-EKE state, (b) the low-EKE state and (c) their difference. All results are calculated from the Global Ocean Reanalysis Simulations Data data set. Hatched areas are significant at the 99% confidence level.

strong KE, especially at its upstream and downstream segments with highest velocity centered on the turning meander at 135°W. As a result, the spatial pattern of the mean flow KE (MKE) exhibits two ribbons distributed along the jet axis. Embedded within the ACC, eddies are correspondingly found to be active and therefore strong EKE is concentrated near the jet (Figure 3c). Peaks of the surface EKE have an S shape centered along the jet axis between 120°W and 150°W. In other words, eddies in the CPSSO are prone to generate and develop in regions with strong background flows, except for the central meander segment where eddies are active in weak currents. This rough collocation between MKE and EKE implies the ACC is an important source of eddy energy in the CPSSO.

Comparing the results obtained from AVISO and GLORYS12V1, we see that the reanalysis well captures the spatial variations of both MKE and EKE, indicative of its reliability in reproducing the large-scale and mesoscale features in the CPSSO. A noticeable difference between the two data sets is that the surface geostrophic EKE in the GLORYS12V1 is significantly larger in magnitude than that in the AVSIO (Figures 3c and 3d). A possible reason is that the gridded AVISO product has been reported to heavily smooth the mesoscale eddies due to the sampling and interpolation procedure (Amores et al., 2018).

The temporal evolution of the EKE displayed in Figure 1d manifests variabilities over different time scales, among which the interannual variability is the most conspicuous feature as suggested by previous studies (Menna et al., 2020; Y. Zhang et al., 2021). Eddy activities are found to greatly increase in 1997, 2001, 2009, 2014, and 2019, whereas drastically decrease in 1993, 1999, 2003, and 2017–2018. In addition, the MKE, which contains the variability from the standing meanders, also exhibits a significant interannual modulation, and its magnitude is comparable to that of the EKE (see Figure S1). It can be also seen that the time series of MKE and EKE are significantly correlated ($r = 0.63$) on the interannual time scale, indicating that the interannual variation of EKE are related to the slowly changing background flow. In the following subsections, we will investigate the dynamical links between the two energy reservoirs, mainly from the perspective of a time-dependent EKE budget analysis. The full budget analysis of the MKE reservoir, which is helpful in understanding the dynamics of the interannual variation of the standing meanders, is not presented in this study thoroughly (it will be the subject of another study). As will be shown in Section 4.2.2, the dominant source of the MKE reservoir is from wind work, indicating that interannual variation of the standing meanders is likely to be modulated by wind forcing.

The composite maps of the depth-integrated EKE and corresponding surface circulations for the two phases are presented in Figures 4a and 4b. Both high and low phases are characterized by elevated EKE level along the meandering jet axis, but with substantial differences in magnitude (Figure 4c). The EKE averaged over the CPSSO in the high-EKE phase (7.49 m^3/s^2) is significantly larger than that in the low-EKE phase (5.65 m^3/s^2). This implies that abundant eddies exist in this region all the time and they have strong variability on the inter-annual scale as shown in Figure 1d. The difference between the two phases (Figure 4c) shows greater values along the jet axis, indicating that the interannual EKE variability is mainly distributed along the AAC jet.

A closer look at the EKE state-mean maps reveals that the ACC in the high- and low-EKE phases has different intensities. Its strength, and hence the MKE (Figure S2) along the jet axis, is greatly reduced from the high to low phases, which implies a close relation of the background jet strength and eddy activity on the interannual time-scale. In the next subsection, we employ the time-dependent energetics analysis as introduced in Section 3 to clarify the contribution of the eddy-mean flow interaction and other processes to the EKE interannual variability in the CPSSO.

4.2. Time-Varying Energetics Analysis

4.2.1. Oceanic Processes

As mentioned in the Introduction, the temporal EKE variability in an ocean sector can be controlled by various mechanisms such as eddy-mean flow interactions triggered by instabilities, non-local advection, wind forcing and etc. In this subsection, we focus on the oceanic (internal) processes. In particular, we will see how the barotropic and baroclinic pathways modulate the interannual EKE variation in the CPSSO. The barotropic pathway is featured by the canonical transfer from the MKE reservoir to the EKE reservoir (i.e., positive $\Gamma_K^{0 \to 1}$ or MKE → EKE) due to barotropic instability. The baroclinic pathway is featured by the canonical transfer from the MAPE reservoir to the EAPE reservoir (i.e., positive $\Gamma_A^{0 \to 1}$ or MAPE → EAPE) and buoyancy conversion from the EAPE reservoir to the EKE reservoir (i.e., positive $-b^1$ or EAPE → EKE) due to baroclinic instability. Temporal evolutions of the depth-integrated EKE and its associated energy terms averaged over the CPSSO (Figure 1a) are displayed in Figure 5. All time series are 1-year low-pass filtered to highlight the interannual variability.

Firstly, for the KE exchange between background currents and mesoscale eddies (MKE → EKE, Figures 5a and 5b), it can be seen that the area-mean $\Gamma_K^{0 \to 1}$ is mostly negative, suggesting that on average eddies transfer their KE back to background flow. Besides, there's no significant simultaneous correlation between the time series of EKE and $\Gamma_K^{0 \to 1}$. However, these results do not necessarily mean that barotropic instability is not responsible for the interannual EKE variation because there is a significant canceling of positive and negative values in the considered region (See Section 4.3 for the spatial patterns). To avoid such an issue, we narrow down the meridional length of the area-averaging box to 100 km and re-calculate the depth-integral. Now the area-mean $\Gamma_K^{0 \to 1}$ is positive and simultaneously correlated with the EKE (dashed lines in Figures 5a and 5b), suggesting that the barotropic pathway indeed plays a non-negligible role in the interannual modulation of EKE. Here we stress that the barotropic pathway is mainly at work in the vicinity of the jet axis.

For the baroclinic pathway (MAPE → EAPE → EKE), both the time series of the area-mean $\Gamma_A^{0 \to 1}$ and $-b^1$ exhibit positive values and nearly simultaneous positive correlation ($r = 0.80$ and $r = 0.87$, respectively) with the EKE, which is statistically significant at a 90% confidence level (Figures 5c–5f). This demonstrates that baroclinic instability controls the EKE variability on the low-frequency time scale.

In addition to barotropic and baroclinic instability processes, non-local processes due to advection and pressure work may also play a role in the EKE energy balance of the regional ocean. Considering the small magnitude of $-\nabla \cdot Q_K^1$ (Table S1 in Supporting Information S1), we examine here the combined effect of the non-local spatial transport term ($-\nabla \cdot Q_K^1$) and the pressure work ($-\nabla \cdot Q_P^1$) term (Figures 5g and 5h). It can be seen that the non-local term is almost negatively correlated to EKE ($r = -0.65$), indicating that the EKE produced by the instability processes is balanced by non-local processes via advection and pressure work. Therefore, nonlocal processes are not the cause of the interannual EKE variability in the CPSSO.

4.2.2. Wind Forcing

In recent decades, attempts have been made to identify the causal relationship between EKE variations in the SO and zonal wind stress variations (Hogg et al., 2015; Marshall et al., 2017; Menna et al., 2020; Meredith & Hogg, 2006; Morrow et al., 2010). As a predominant external trigger for SO circulation, wind forcing has been considered as a major mechanism for the mesoscale eddy variability. To investigate the response of the regional eddies to the wind forcing over it, here, we diagnose the wind work on the background flow window (WW^0) and the eddy window (WW^1) using Equation 8. Figures 6a and 6b display the climatological spatial distributions of WW^1 and WW^0, respectively. A positive (negative) value denotes gains (loss) of KE from (to) the atmospheric wind stress. It can be seen that WW^1 is generally negative (Figure 6a), indicating that wind stress can directly suppress the development of the mesoscale eddies, that is, the well-known "eddy-killing" process (e.g., Renault et al., 2017). In addition, this term has a significantly simultaneous negative correlation with EKE ($r = -0.79$,
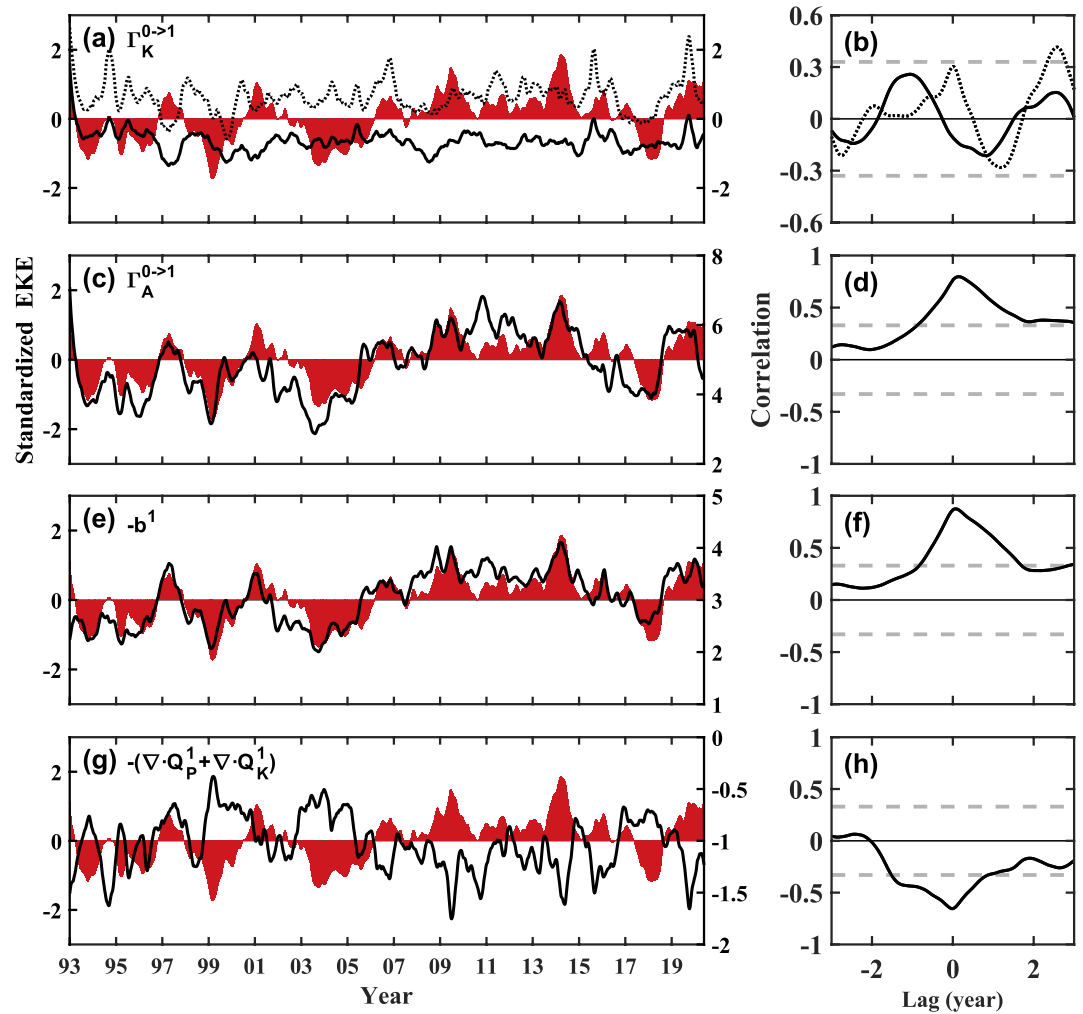
Figure 5. (a) Time series of the standardized depth-integrated (0–1000-m) Eddy kinetic energy (EKE) (red bar) and $\Gamma_K^{0\rightarrow1}$ (solid black line; 10^{-6} m^3/s^3) averaged over the central Pacific sector of the Southern Ocean based on the Global Ocean Reanalysis Simulations Data data set. Both time series are 1-year low-pass filtered. (b) Lagged correlation between EKE and $\Gamma_K^{0\rightarrow1}$. A positive lag means that $\Gamma_K^{0\rightarrow1}$ leads EKE. The dashed gray lines indicate the 90% confidence level. Panels (c), (d) as in panels (a), (b), but for $\Gamma_A^{0\rightarrow1}$. Panels (e), (f) as in panels (a), (b), but for $-b^1$. Panels (g), (h) as in panels (a), (b), but for $-\left(\nabla \cdot Q_P^1 + \nabla \cdot Q_K^1\right)$. Dashed black line in panel (a) shows the time series of area-mean $\Gamma_K^{0\rightarrow1}$ (unit: 10^{-5} m^3/s^3) when narrowing down the meridional length of the area-averaging box to 100 km.

Figures 6c and 6d), suggesting that the direct wind work functions as a simultaneous energy sink for the eddy variability.

It is well known that the wind power input mainly goes into the large-scale current (Wunsch, 1998). From Figures 6b and 6e, we can see that the magnitude of WW^0 is about two orders of magnitude larger than WW^1, indicating that the wind power mainly fuels the MKE reservoir in this region, consistent with previous findings. By performing lead-lag correlation analysis, we find that the correlation coefficient between WW^0 and EKE reaches its maximum when WW^0 leads EKE by ∼1–3.5 years (Figure 6f). This time lag is consistent with previous findings that the wind stress change usually leads the EKE in the SO by 1–3 years (Hogg et al., 2015; Meredith & Hogg, 2006; Morrow et al., 2010). Now a natural question to ask is how does the external wind work on the background flow modulate the EKE? To answer this question, we show in Figure 7 the pathway of wind power input in the energy cycle. It can be seen that the wind power input is the dominant source of the MKE reservoir, whereas non-local processes term ($-\nabla \cdot \left(Q_K^0 + Q_P^0\right)$) acts as a major sink of the MKE reservoir.

It is worth noting that the energy conversion from the MKE reservoir to the MAPE reservoir (i.e., positive b^0 or MKE → MAPE) is much smaller in magnitude than that of the wind power input (Figure 7). This result seems
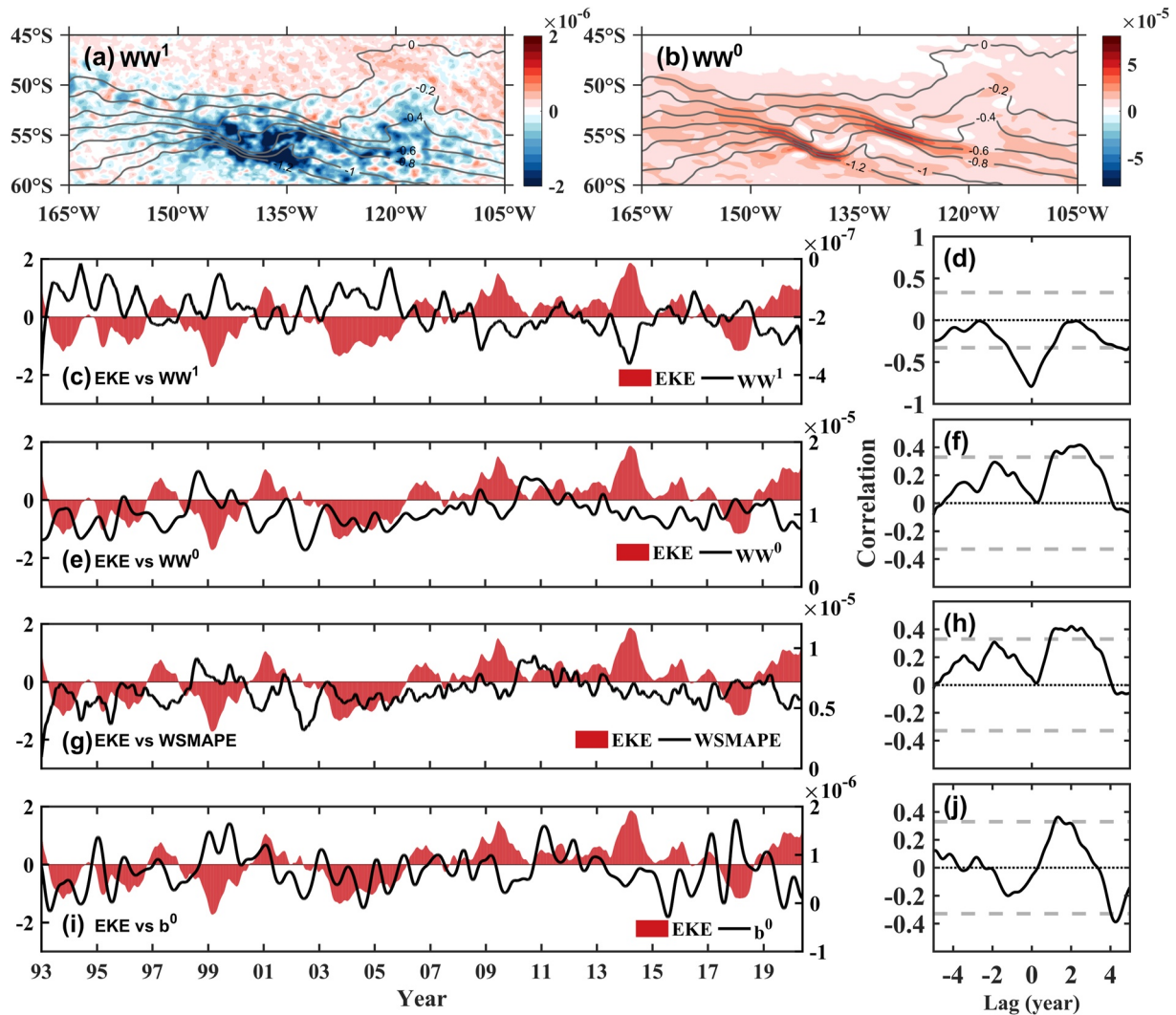
Figure 6. (a) Long-term mean maps of the wind work on the eddy window (WW^1) (colored shading; m^3/s^3) calculated from ERA (ERA-Interim and ERA5) wind stress and sea surface height (contours, m) (b) Same as in panel (a), but for the wind work on the background flow (WW^0). Panels (c), (d) as in panels (a), (b) in Figure 5, but for WW^1. Panels (e), (f) as in panels (c), (d), but for WW^0. Panels (g), (h) as in panels (c), (d), but for WSMAPE. Panels (i), (j) as in panels (c), (d), but for b^0.

inconsistent with the classical oceanic Lorenz energy cycle in which the wind-driven mean current converts its KE to MAPE by Ekman pumping process and the MAPE is further released to energize mesoscale eddies via the baroclinic pathway. This puzzling feature is actually because the b^0 term is heavily dependent on the choice of reference density, which is chosen as the time-mean and area-mean density over the CPSSO sector. To tackle this problem, Matsuta and Masumoto (2023) proposed that the MAPE reservoir built up by the wind stress can be approximately estimated by wind power input to the mean geostrophic currents, which is independent of the reference state. Following Matsuta and Masumoto (2023), we estimated the MAPE gain due to the wind forcing (denoted as WSMAPE) in the CPSSO, which on average accounts for about 63% of the total wind power input to the background flow in this region. Since the temporal variations of the WSMAPE and WW^0 are almost identical, it is not surprising that the WSMAPE also leads the regional EKE by about 1–3.5 years (Figure 6e–6h). It is interesting to note that although the magnitude of b^0 is largely underestimated, its temporal variation seems reasonable as it shows significant positive correlation with the EKE time series by a lead time of 1–2 years (Figures 6i and 6j), indicating that the MKE is indeed converted to the MAPE through Ekman pumping process.

The gained MAPE is then released to EAPE through baroclinic instability (MAPE → EAPE), of which about 63% is further converted to EKE through buoyancy conversion (EAPE → EKE, Figure 7). In contrast to the baroclinic pathway, the barotropic pathway (MKE → EKE) does not seem to be at work from a domain-averaged perspective.
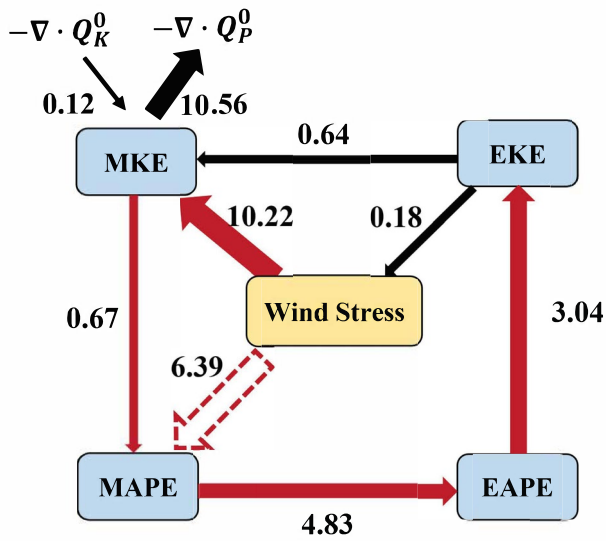
Figure 7. A schematic diagram showing the pathway of wind power input in the oceanic Lorenz energy cycle. The numbers related to the wind stress are the area-mean of wind works over the central Pacific sector of the Southern Ocean. Other numbers are obtained by calculating the area-mean and depth-integral (0–1,000 m) of each energy term in the diagram. The dashed arrow denotes the estimation of MAPE gain due to wind stress following Matsuta and Masumoto (2023). The units are all in 10^{-6} m^3/s^3.

The direction of KE transfer is in an upscale sense (i.e., EKE → MKE) when considering the area-mean over the CPSSO (Figures 5a and 7). However, the barotropic instability is mainly confined to the jet axis, especially west of 142°W (see Section 4.3), resulting in a rather localized pattern of MKE → EKE. The above results show that the wind forcing affects the inter-annual EKE variability in the CPSSO region mainly through the baroclinic pathway, that is, MKE → MAPE → EAPE → EKE.

To see whether the temporal changes of wind works depend significantly on the wind product, we also used wind stress data from the National Centers for Environmental Prediction Climate Forecast System Reanaly-sis (NCEP-CFSR, Saha et al., 2010) and found that both the spatial pattern and interannual variation are similar to the results using the ERA product (not shown). This suggests that the delayed relation between the interannual changes of wind forcing and EKE as found in this study is robust.

4.3. Spatial Variations

The time-series analyses shown in Figures 5 and 6 clarify different physical processes controlling the interannual variability of the EKE in the CPSSO. In this subsection we further extend the analysis to a spatial-dependent perspec-tive by presenting the composite maps of each energy term for the high- and low-EKE phases.

Figure 8 displays the composite maps of the EKE-associated terms vertically integrated from 0 to 1,000 m. To better show the variations along the jet axis where the EKE co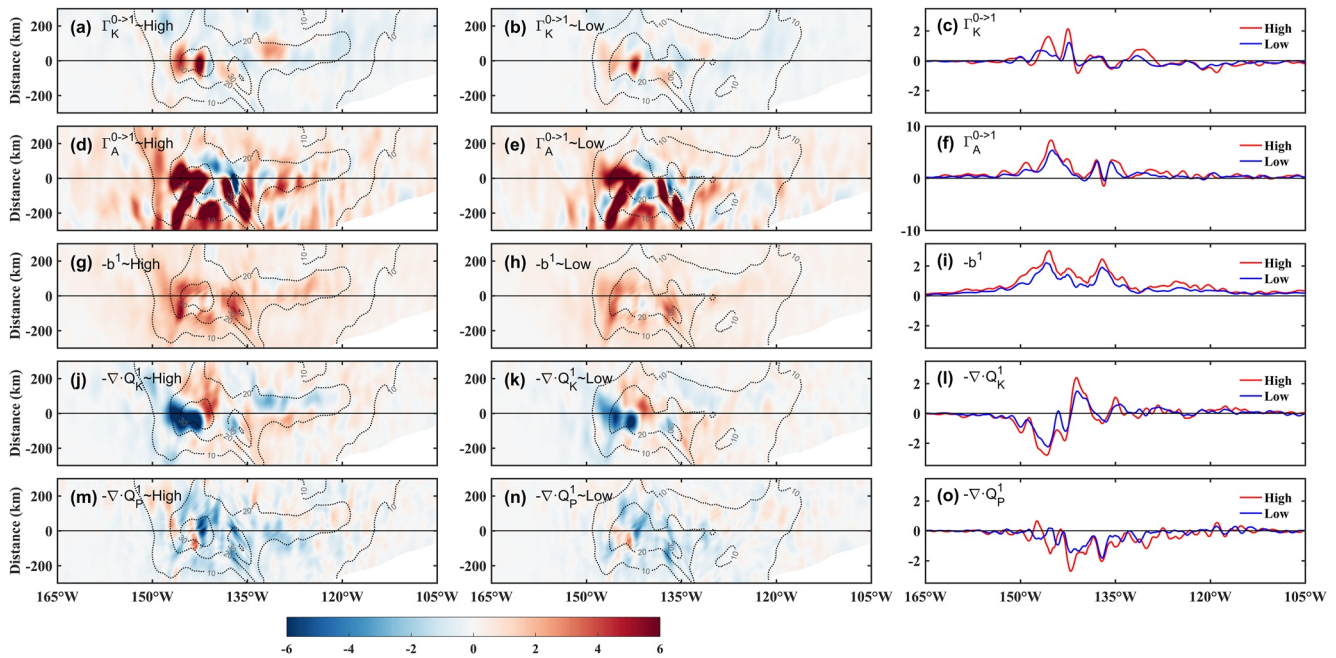ncentrates, here we use a jet-following coordinate as introduced in Delman et al. (2015). Figures 8a and 8b show the horizontal maps of the depth-integrated (upper 1,000 m) $\Gamma_K^{0 \to 1}$ for the high and low composites, respectively. The metric, when positive, is a measure of KE transfer from the background flow to eddies as introduced in Section 3. $\Gamma_K^{0 \to 1}$ always has the strongest signals along the jet axis and decreases away from it. The positive $\Gamma_K^{0 \to 1}$ near the jet axis indicates that the currents here are barotropically unstable, transferring KE to eddies via barotropic pathway (MKE → EKE). The nega-tive $\Gamma_K^{0 \to 1}$ away from the jet axis indicates an inverse cascade that eddies return KE to the background flow to maintain it. This scenario is intensified in the high-EKE phase and weakened in the low-EKE phase, suggest-ing that the barotropically unstable jet provides more KE to fuel the eddies which leads to high EKE and vice versa. According to the meridionally averaged results (Figure 8c), $\Gamma_K^{0 \to 1}$ is stronger during the high-EKE state than during the low-EKE state in most segments along the jet. For the most unstable segment located at around 142°W, $\Gamma_K^{0 \to 1}$ in the high-EKE state (2.26×10^{-5} m^3/s^3) can be 2.4 times as strong as that in the low-EKE state (0.96×10^{-5} m^3/s^3). These results suggest the importance of barotropic instability to the variation of EKE in this region.

Another well-known mechanism of eddy energy generation is baroclinic instability which is measured by the metric $\Gamma_A^{0 \to 1}$ (Figures 8d and 8e). Although mingled with some negative patches, the $\Gamma_A^{0 \to 1}$ pattern exhibits overall positive values in the CPSSO, indicative of the occurrence of baroclinic instability which energize the eddies via the release of APE deposited in the background flow. Comparison between the two composites shows that the baroclinic instability has higher intensity in the high-EKE state than in the low-EKE state, indicating that the jet is more baroclinically unstable and releases more APE to the eddies in the high-EKE state (Figures 8d and 8e). Notice the above-mentioned APE-transfer process (i.e., MAPE → EAPE) is the first phase of baroclinic pathway. The second phase of baroclinic instability, namely, EAPE → EKE, is quanti-fied by $-b^1$, and is shown in Figures 8g–8i. Here positive $-b^1$ indicates a conversion from EAPE to EKE. As shown in Figures 8g and 8h, $-b^1$ is stronger in the high-EKE state, indicating that a larger amount of EAPE is converted into EKE. It is worth mentioning that not all of the EAPE transferred from MAPE is converted to EKE. In the CPSSO, the convention ratio ($-b^1/\Gamma_A^{0 \to 1}$) is smaller than 70%. From the above analysis, we find that the baroclinic pathway (MAPE → EAPE → EKE) is stronger during the high-EKE state, again indicating that baroclinic instability plays an important role in modulating the interannual variation of the EKE in the CPSSO.

Figure 8. Jet frames of depth-integrated (upper 1,000 m) $\Gamma_K^{0\to1}$ (colored shading; 10^{-5} m³/s³) in the (a) high-EKE phase and (b) low-EKE phase and (c) meridional-mean structures within 200 km calculated from the Global Ocean Reanalysis Simulations Data data set. Eddy kinetic energy composites (contours; m²/s²) in each phase are superposed in panels (a) and (b). Panels (d), (e), (f) as in panels (a), (b), (c), but for $\Gamma_A^{0\to1}$. Panels (g), (h), (i) as in panels (a), (b), (c), but for $-b^1$. Panels (j), (k), (l) as in panels (a), (b), (c), but for $-\nabla \cdot Q_K^1$. Panels (m), (n), (o) as in panels (a), (b), (c), but for $-\nabla \cdot Q_P^1$.

In addition to the above-mentioned instability processes, other processes such as non-local EKE transport and pressure work, could also contribute to the EKE balance. The spatial distribution of the EKE flux divergence ($-\nabla \cdot Q_K^1$) at two phases are shown in Figures 8j and 8k, respectively. Positive (negative) $-\nabla \cdot Q_K^1$ means an increase (decrease) of local EKE due to the convergence (divergence) of the EKE caused by advection processes. As shown in Figures 8j and 8k, the $-\nabla \cdot Q_K^1$ is dominantly negative in the upstream region (west of 140°W) and positive in the downstream region. This means that the EKE is advected from the upstream to the downstream. Recall that the strengths of barotropic and baroclinic instabilities maximize in the upstream region. This means that $-\nabla \cdot Q_K^1$ mainly works to redistribute EKE in the considered domain. Indeed, from Figure 8l, we can see that there is a strong cancellation of the positive and negative values in the upstream and downstream regions. As for $-\nabla \cdot Q_P^1$ (Figures 8m–8o), it is generally negative in both phases, indicating that the pressure work is a sink for EKE in the CPSSO. The meridionally averaged $-\nabla \cdot Q_P^1$ in Figure 8o shows that the pressure work is stronger in the high-EKE phase than in the low-EKE phase, indicating that more EKE is redistributed in the high-EKE phase.

To better understand the contribution of each term to the variation of the EKE, the vertical structures of the energetics during the two different states are presented in Figure 9. A significant feature is that all these energy terms have larger amplitudes during the high-EKE state than in the low-EKE state. Another feature is that these terms have different vertical structures. $\Gamma_K^{0\to1}$ has a surface-trapped structure (Figures 9a and 9b), while $\Gamma_A^{0\to1}$ and $-b^1$ maximize in the subsurface layer (around 600 m; Figures 9c–9f). This indicates that the KE exchange between background flow and mesoscale eddies is the dominant EKE generation mechanism in the surface layer, especially above 200 m where EKE production through baroclinic instability is considerably weak. The baroclinic instability dominates the EKE generation in the subsurface layer where the main thermocline of the AAC resides. The generated EKE by the two instabilities is advected downstream by the mean jet (Figures 9g and 9h). It is interesting to note that the pressure work ($-\nabla \cdot Q_P^1$) is negative in the subsurface layer and positive in the near surface, indicating that the EKE is transported vertically from the subsurface to the surface (Figures 9i and 9j). A similar upward EKE transport feature is also reported in the upstream Kuroshio Extension (Yang et al., 2021). This means that the strong EKE signals trapped in the surface mixed layer have two major sources. One is barotropic instability as mentioned before, another is upward energy flux from the baroclinic instability-dominated subsurface layer. The contribution from baroclinic instability can even exceed barotropic instability in the downstream
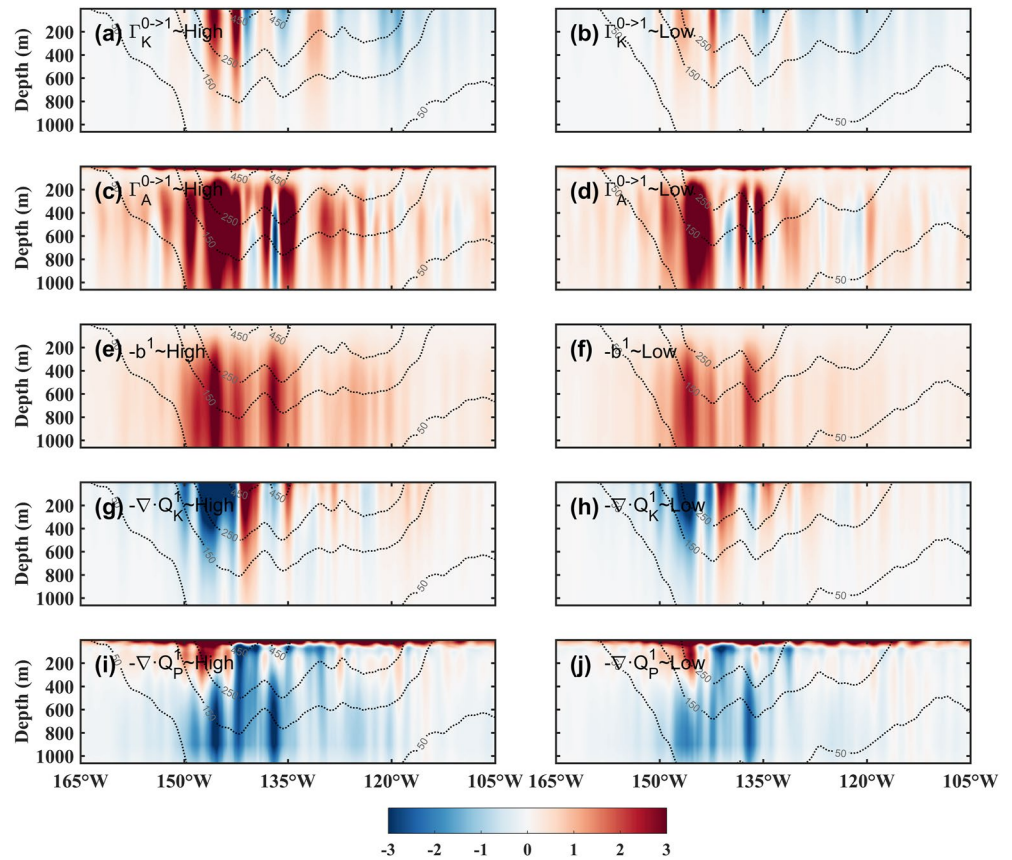
Figure 9. Vertical distributions of $\Gamma_K^{0\to1}$ (colored shading; 10^{-8} m^2/s^3) and Eddy kinetic energy (contours; cm^2/s^2) averaged within 200 km of the jet axis in the (a) high-EKE phase and (b) low-EKE phase based on Global Ocean Reanalysis Simulations Data data set. Panels (c), (d) as in panels (a), (b), but for $\Gamma_A^{0\to1}$. Panels (e), (f) as in panels (a), (b), but for $-b^1$. Panels (g), (h) as in panels (a), (b), but for $-\nabla \cdot Q_K^1$. Panels (i), (j) as in panels (a), (b), but for $-\nabla \cdot Q_P^1$.

region where the EKE is found to transfer back to the MKE reservoir. The above analyses further demonstrate the dominant role of the baroclinic energy pathway in the EKE change from a spatial-dependence perspective.

5. Conclusions and Discussions

In this study, we investigate the dynamical processes related to the interannual variability in the central Pacific sector of the Southern Ocean (CPSSO) by a recently developed tool, MWT, and the MWT-based theory of canonical transfer over the 1993–2020 period. Using the MWT, the original fields are decomposed into subfields on a nonstationary background flow window (periods >192 days) and an eddy window (periods <192 days). The orthogonality and localization of the MWT not only allow us to further investigate the time-varying characteristics of the KE in the eddy window, but also quantify the role of different mechanisms in the EKE variations on the interannual time scale. The results show that significant interannual EKE variability exists in the CPSSO. The EKE shows high anomaly values in 1997, 2001, 2009, 2014, and 2019, whereas low anomaly in 1993, 1999, 2003, and 2017–2018.

By diagnosing the canonical transfers between the background flow window and the eddy window, and the non-local processes, the relative contributions from oceanic processes to the interannual eddy variability are quantified. The diagnostic results indicate that the baroclinic energy pathway (MAPE → EAPE → EKE) associated with the baroclinic instability and the barotropic energy pathway (MKE → EKE) associated with barotropic instability are the two dominant sources of EKE in this region, with the baroclinic pathway taking the leading role. Different from the baroclinic instability, barotropic instability is more concentrated along the jet axis and only prominent in the upstream portion of our considered domain. Non-local processes such as pressure work and advection act to dampen the EKE gained from the two instability processes.

The interannual variability of the external wind work done to the eddies and the background flow are also examined. Comparing to the instability processes, the direct work of wind stress on eddies only makes a small contribution to the interannual variability of EKE. In contrast, we find that the wind forcing affects the interannual EKE variation via two indirect pathways. The wind first transfers energy to MKE, which is then converted to MAPE and finally released to EKE through baroclinic instability (MKE → MAPE → EAPE → EKE). Another pathway in which MKE directly fuels EKE via barotropic instability (MKE → EKE) is also responsible for the interannual EKE variation, though with a smaller contribution compared to the baroclinic pathway. The time lag of the response of EKE to the wind power input is about 1–3.5 years, consistent with previous findings (Hogg et al., 2015; Meredith & Hogg, 2006; Morrow et al., 2010).

In the present study, we have shown the time-dependent energy pathways by which the wind power injection affects the interannual EKE variation in the CPSSO sector. However, we did not analyze in this study the mechanism underlying the long-term increasing trend of the EKE on the decadal and multi-decadal scales, which is another topic of wide interest in the field (Hogg et al., 2015; Zhang et al., 2021). The MWT-based time-varying energetics framework used in this study can also be applied to investigate such a problem. We will leave it for future investigation. Due to the horizontal resolution of the GLORYS12V1 simulation, the submesoscale processes are not resolved and thus not considered in the present study. Recent modeling study by Zhang et al. (2023) has found that inverse energy cascade from the submesoscale plays an important role in the mesoscale EKE budget and thus regulate the eddy meridional heat transport the SO. The role of submesoscale processes in the multiscale interactions in the SO will be discussed in the future study with the help of higher resolution data. Finally, the present study only focuses on the dynamics of EKE variability controlled by the local wind forcing, the relative importance of local and remote forcings (e.g., the El Niño-Southern Oscillation) in modulating the temporal EKE variability deserves further investigation.

Data Availability Statement

AVISO data set is available at Centre national d'études spatiales (CNES, https://www.aviso.altimetry.fr/en/data/data-access/aviso-cnes-data-center.html) (AVISO, 2019). GLORYS12V1 data set is available at Copernicus Marine and Environment Monitoring Service (CMEMS, https://data.marine.copernicus.eu/product/GLOBAL_MULTIYEAR_PHY_001_030/description) (GLORYS12V1, 2022). ERA-Interim and ERA5 data sets are available at https://apps.ecmwf.int/datasets/data/interim-full-daily and https://cds.climate.copernicus.eu/cdsapp#!/dataset/reanalysis-era5-single-levels?tab=form, separately (ERA5, 2023). NCEP-CFSR data set is available at https://www.hycom.org/dataserver/ncep-cfsr. The MS-EVA software is available online (http://www.ncoads.cn/) (MS-EVA, 2016).

References

Abernathey, R., & Cessi, P. (2014). Topographic enhancement of eddy efficiency in Baroclinic Equilibration. *Journal of Physical Oceanography*, *44*(8), 2107–2126. https://doi.org/10.1175/JPO-D-14-0014.1

Amores, A., Jordà, G., Arsouze, T., & Le Sommer, J. (2018). Up to what extent can we characterize ocean eddies using present-day gridded altimetric products? *Journal of Geophysical Research: Oceans*, *123*(10), 7220–7236. https://doi.org/10.1029/2018JC014140

AVISO. (2019). Global ocean gridded L4 sea surface heights and derived variables reprocessed 1993 ongoing [Dataset]. E.U Copernicus Marine and Environment Monitoring Service (CMEMS), Marine Data Store (MDS). https://doi.org/10.48670/moi-00148

Barthel, A., Hogg, A. M., Waterman, S., & Keating, S. (2022). Baroclinic control of southern ocean eddy upwelling near topography. *Geophysical Research Letters*, *49*(7), e2021GL097491. https://doi.org/10.1029/2021GL097491

Barthel, A., McC. Hogg, A., Waterman, S., & Keating, S. (2017). Jet–topography interactions affect energy pathways to the deep Southern Ocean. *Journal of Physical Oceanography*, *47*(7), 1799–1816. https://doi.org/10.1175/JPO-D-16-0220.1

Bischoff, T., & Thompson, A. F. (2014). Configuration of a Southern Ocean storm track. *Journal of Physical Oceanography*, *44*(12), 3072–3078. https://doi.org/10.1175/JPO-D-14-0062.1

Cai, Y., Chen, D., Mazloff, M. R., Lian, T., & Liu, X. (2022). Topographic modulation of the wind stress impact on eddy activity in the Southern Ocean. *Geophysical Research Letters*, *49*(13), e2022GL097859. https://doi.org/10.1029/2022GL097859

Chapman, C. C., Hogg, A. M. C., Kiss, A. E., & Rintoul, S. R. (2015). The dynamics of Southern Ocean storm tracks. *Journal of Physical Oceanography*, *45*(3), 884–903. https://doi.org/10.1175/JPO-D-14-0075.1

Delman, A. S., McClean, J. L., Sprintall, J., Talley, L. D., Yulaeva, E., & Jayne, S. R. (2015). Effects of eddy vorticity forcing on the mean state of the Kuroshio extension. *Journal of Physical Oceanography*, *45*(5), 1356–1375. https://doi.org/10.1175/JPO-D-13-0259.1

Ducet, N., Le Traon, P. Y., & Reverdin, G. (2000). Global high-resolution mapping of ocean circulation from TOPEX/Poseidon and ERS-1 and -2. *Journal of Geophysical Research*, *105*(C8), 19477–19498. https://doi.org/10.1029/2000JC900063

ERA5. (2023). ERA5 hourly data on single levels from 1940 to present [Dataset]. E.U Copernicus Marine Service Information (CMEMS), Marine Data Store (MDS). https://doi.org/10.24381/cds.adbb2d47

Frenger, I., Münnich, M., Gruber, N., & Knutti, R. (2015). Southern Ocean eddy phenomenology. *Journal of Geophysical Research: Oceans*, *120*(11), 7413–7449. https://doi.org/10.1002/2015JC011047

Fu, L.-L., Chelton, D., Le Traon, P.-Y., & Morrow, R. (2010). Eddy dynamics from satellite altimetry. *Oceanography*, *23*(4), 14–25. https://doi.org/10.5670/oceanog.2010.02

GLORYS12V1. (2022). Global ocean physical multi year product [Dataset]. Copernicus Marine and Environment Monitoring Service (CMEMS). https://doi.org/10.48670/moi-00021

Grooms, I., Nadeau, L.-P., & Smith, K. S. (2013). Mesoscale eddy energy locality in an idealized ocean model. *Journal of Physical Oceanography*, *43*(9), 1911–1923. https://doi.org/10.1175/JPO-D-13-036.1

Held, I. M. (1983). Stationary and quasi-stationary eddies in the extratropical troposphere: Theory. *Large-Scale Dynamical Processes in the Atmosphere*, 127–168.

Hogg, A. M. C., & Blundell, J. R. (2006). Interdecadal variability of the Southern Ocean. *Journal of Physical Oceanography*, *36*(8), 1626–1645. https://doi.org/10.1175/JPO2934.1

Hogg, A. M. C., Meredith, M. P., Chambers, D. P., Abrahamsen, E. P., Hughes, C. W., & Morrison, A. K. (2015). Recent trends in the Southern Ocean eddy field. *Journal of Geophysical Research: Oceans*, *120*(1), 257–267. https://doi.org/10.1002/2014JC010470

Hogg, A. M. C., Penduff, T., Close, S. E., Dewar, W. K., Constantinou, N. C., & Martínez-Moreno, J. (2022). Circumpolar variations in the chaotic nature of Southern Ocean eddy dynamics. *Journal of Geophysical Research: Oceans*, *127*(5). https://doi.org/10.1029/2022JC018440

Huang, M., Yang, Y., & Liang, X. (2023). Seasonal eddy variability in the northwestern tropical Atlantic Ocean. *Journal of Physical Oceanography*, *53*(4), 1069–1085. https://doi.org/10.1175/JPO-D-22-0200.1

Hughes, C. W. (2005). Nonlinear vorticity balance of the Antarctic circumpolar current. *Journal of Geophysical Research*, *110*(C11), C11008. https://doi.org/10.1029/2004JC002753

Kang, D., & Curchitser, E. N. (2017). On the evaluation of seasonal variability of the ocean kinetic energy. *Journal of Physical Oceanography*, *47*(7), 1675–1683. https://doi.org/10.1175/JPO-D-17-0063.1

Liang, X. S. (2016). Canonical transfer and multiscale energetics for primitive and quasigeostrophic atmospheres. *Journal of the Atmospheric Sciences*, *73*(11), 4439–4468. https://doi.org/10.1175/JAS-D-16-0131.1

Liang, X. S., & Anderson, D. G. M. (2007). Multiscale window transform. *Multiscale Modeling and Simulation*, *6*(2), 437–467. https://doi.org/10.1137/06066895X

Liang, X. S., & Robinson, A. R. (2005). Localized multiscale energy and vorticity analysis. *Dynamics of Atmospheres and Oceans*, *38*(3–4), 195–230. https://doi.org/10.1016/j.dynatmoce.2004.12.004

Lin, X., Zhai, X., Wang, Z., & Munday, D. R. (2018). Mean, variability, and trend of Southern Ocean wind stress: Role of wind fluctuations. *Journal of Climate*, *31*(9), 3557–3573. https://doi.org/10.1175/JCLI-D-17-0481.1

Marshall, D. P., Ambaum, M. H. P., Maddison, J. R., Munday, D. R., & Novak, L. (2017). Eddy saturation and frictional control of the Antarctic circumpolar current: Eddy saturation of the ACC. *Geophysical Research Letters*, *44*(1), 286–292. https://doi.org/10.1002/2016GL071702

Matsuta, T., & Masumoto, Y. (2023). Energetics of the Antarctic circumpolar current. Part I: The Lorenz energy cycle and the vertical energy redistribution. *Journal of Physical Oceanography*, *53*(6), 1467–1484. https://doi.org/10.1175/JPO-D-22-0133.1

Menna, M., Cotroneo, Y., Falco, P., Zambianchi, E., Di Lemma, R., Poulain, P.-M., et al. (2020). Response of the Pacific sector of the Southern Ocean to wind stress variability from 1995 to 2017. *Journal of Geophysical Research: Oceans*, *125*(10). https://doi.org/10.1029/2019JC015696

Meredith, M. P., & Hogg, A. M. (2006). Circumpolar response of Southern Ocean eddy activity to a change in the southern annular mode. *Geophysical Research Letters*, *33*(16), L16608. https://doi.org/10.1029/2006GL026499

Morrow, R., Ward, M. L., Hogg, A. M. C., & Pasquet, S. (2010). Eddy response to Southern Ocean climate modes. *Journal of Geophysical Research*, *115*(C10), 2009JC005894. https://doi.org/10.1029/2009JC005894

MS-EVA. (2016). Localized multiscale energy and vorticity analysis [Software]. NCOADS. Retrieved from http://www.ncoads.cn/

Renault, L., McWilliams, J. C., & Masson, S. (2017). Satellite observations of imprint of oceanic current on wind stress by air-sea coupling. *Scientific Reports*, *7*(1), 17747. https://doi.org/10.1038/s41598-017-17939-1

Saha, S., Moorthi, S., Pan, H.-L., Wu, X., Wang, J., Nadiga, S., et al. (2010). The NCEP climate forecast system reanalysis. *Bulletin of the American Meteorological Society*, *91*(8), 1015–1058. https://doi.org/10.1175/2010BAMS3001.1

Sallée, J.-B., Morrow, R., & Speer, K. (2008). Eddy heat diffusion and subAntarctic mode water formation. *Geophysical Research Letters*, *35*(5), L05607. https://doi.org/10.1029/2007GL032827

Sokolov, S., & Rintoul, S. R. (2009). Circumpolar structure and distribution of the Antarctic circumpolar current fronts: 1. Mean circumpolar paths. *Journal of Geophysical Research*, *114*(C11), C11018. https://doi.org/10.1029/2008JC005108

von Storch, J.-S., Eden, C., Fast, I., Haak, H., Hernández-Deckers, D., Maier-Reimer, E., et al. (2012). An estimate of the Lorenz energy cycle for the World Ocean based on the STORM/NCEP simulation. *Journal of Physical Oceanography*, *42*(12), 2185–2205. https://doi.org/10.1175/JPO-D-12-079.1

Strang, G., & Nguyen, T. (1996). *Wavelets and filter banks*. SIAM.

Straub, D. N. (1993). On the transport and angular momentum balance of channel models of the Antarctic circumpolar current. *Journal of Physical Oceanography*, *23*(4), 776–782. https://doi.org/10.1175/1520-0485(1993)023<0776:OTTAAM>2.0.CO;2

Tamsitt, V., Talley, L. D., Mazloff, M. R., & Cerovečki, I. (2016). Zonal variations in the Southern ocean heat budget. *Journal of Climate*, *29*(18), 6563–6579. https://doi.org/10.1175/JCLI-D-15-0630.1

Thompson, A. F., & Sallée, J.-B. (2012). Jets and topography: Jet Transitions and the impact on transport in the Antarctic circumpolar current. *Journal of Physical Oceanography*, *42*(6), 956–972. https://doi.org/10.1175/JPO-D-11-0135.1

Williams, R. G., Wilson, C., & Hughes, C. W. (2007). Ocean and atmosphere storm tracks: The role of eddy vorticity forcing. *Journal of Physical Oceanography*, *37*(9), 2267–2289. https://doi.org/10.1175/JPO3120.1

Wilson, C., Hughes, C. W., & Blundell, J. R. (2015). Forced and intrinsic variability in the response to increased wind stress of an idealized Southern Ocean. *Journal of Geophysical Research: Oceans*, *120*(1), 113–130. https://doi.org/10.1002/2014JC010315

Wunsch, C. (1998). The work done by the wind on the oceanic general circulation. *Journal of Physical Oceanography*, *28*(11), 2332–2340. https://doi.org/10.1175/1520-0485(1998)028<2332:TWDBTW>2.0.CO;2

Xu, C., Zhai, X., & Shang, X.-D. (2016). Work done by atmospheric winds on mesoscale ocean eddies: Wind work on ocean eddies. *Geophysical Research Letters*, *43*(23). https://doi.org/10.1002/2016GL071275

Xu, X., Liu, J., & Huang, G. (2022). Understanding sea surface temperature cooling in the Central-East Pacific sector of the Southern Ocean during 1982–2020. *Geophysical Research Letters*, *49*(10). https://doi.org/10.1029/2021GL097579

Yang, Y., Liang, X. S., & Sasaki, H. (2021). Vertical coupling and dynamical source for the intraseasonal variability in the deep Kuroshio Extension. *Ocean Dynamics*, *71*(11–12), 1069–1086. https://doi.org/10.1007/s10236-021-01482-9

Youngs, M. K., Thompson, A. F., Lazar, A., & Richards, K. J. (2017). ACC meanders, energy transfer, and mixed barotropic–baroclinic instability. *Journal of Physical Oceanography*, *47*(6), 1291–1305. https://doi.org/10.1175/JPO-D-16-0160.1

Zhang, Y., Chambers, D., & Liang, X. (2021). Regional trends in Southern Ocean eddy kinetic energy. *Journal of Geophysical Research: Oceans*, *126*(6). https://doi.org/10.1029/2020JC016973

Zhang, Z., Liu, Y., Qiu, B., Luo, Y., Cai, W., Yuan, Q., et al. (2023). Submesoscale inverse energy cascade enhances Southern Ocean eddy heat transport. *Nature Communications*, *14*(1), 1335. https://doi.org/10.1038/s41467-023-36991-2